Journal of Petroleum Science and Engineering 196 (2021) 107651

Contents lists available at ScienceDirect

Journal of Petroleum Science and Engineering

journal homepage: http://www.elsevier.com/locate/petrol

CO_2 mobility reduction using foam stabilized by CO_2- and water-soluble surfactants

T. Føyen [a,b,*], Z.P. Alcorn [a], M.A. Fernø [a], A. Barrabino [b], T. Holt [b]

[a] Department of Physics and Technology University of Bergen, Norway
[b] SINTEF Industry, Norway

ARTICLE INFO

Keywords:
CO_2 foam
CO_2 EOR
CO_2 storage
CCUS
Surfactants
Mobility control

ABSTRACT

Foam can reduce CO_2 mobility to improve the sweep efficiency during injection into subsurface geological formations for CO_2 storage and enhanced oil recovery. However, CO_2 foams are thermodynamically unstable, so they must be stabilized. Surfactants are often used to generate and stabilize foams in porous media and can be soluble in the aqueous phase, or in the CO_2 phase. Aqueous- and CO_2-soluble surfactants must be characterized for their ability to reduce CO_2 mobility and stabilize foam at reservoir conditions. In addition, numerical models are necessary to predict and evaluate the effect of foam for field-scale applications and require empirical data obtained from core-scale flooding experiments. This study presents a series of steady-state foam co-injections with dense phase CO_2 and either aqueous- or CO_2-soluble surfactant solutions at varying CO_2 flow velocities and CO_2 fractions. One anionic water-soluble surfactant, which is considered a benchmark foam stabilizer, and five partially CO_2-soluble non-ionic surfactants were investigated. Gamma ray attenuation was used to accurately monitor *in-situ* saturations during steady-state co-injections. The primary objective was to determine the steady-state foam characteristics of the different surfactants by evaluating the mobility reduction factor (MRF) and the limiting water saturation where foam abruptly collapses (S_w^*). All of the tested surfactants generated foam and reduced CO_2 mobility by more than three orders of magnitude. The anionic surfactant increased foam stability at lower water saturations, compared to the non-ionic surfactants, which resulted in lower residual water saturations and increased pore volume available for CO_2 storage. Core flooding results provided input into a local-equilibrium foam model. The fitted foam model reproduced the experimental results for the anionic surfactant and for three of the five non-ionic surfactants. The two latter non-ionic surfactants violated model assumptions because non-monotonic water saturation changes were observed, an effect not accurately captured by local-equilibrium foam models. However, the modelling work elucidated subtle experimental trends and demonstrated the applicability of the dataset as input into implicit-texture local-equilibrium foam models.

1. Introduction

Large-scale CO_2 storage in subsurface geologic formations is required to achieve the emission goals of limiting global warming to 1.5 °C (IPPC, 2014). The bulk of CO_2 emissions are from hydrocarbon combustion and industrial activities. Despite the need to reduce CO2 emissions, a drastic reduction in hydrocarbon production is not expected in the next decades (IEA, 2018). Therefore, technologies must be developed to provide reliable, available and affordable energy with reduced carbon footprint. Lifecycle CO_2 emissions from hydrocarbons can be significantly reduced by utilizing captured anthropogenic CO_2 for enhanced oil recovery (EOR), where CO_2 is used as a commodity to extract remaining oil from depleted reservoirs and is simultaneously stored (Lake et al., 2014). CO_2 EOR can provide a cost-efficient method for establishing the necessary infrastructure for large-scale projects when co-optimized for both oil production and CO_2 storage (Ettehadtavakkol et al., 2014; Lindeberg et al., 2017). Over 40 years of CO_2 EOR experience in the US shows mixed results due to poor sweep efficiency caused by the high mobility of CO_2 at reservoir conditions, relative to oil and brine. Poor sweep efficiencies are also amplified by reservoir heterogeneities (Lee and Kam, 2013) because injected CO_2 may flow through the highest permeability layers and/or fractures.

CO_2 foam mobility control can mitigate poor sweep efficiencies during CO_2 EOR and CO_2 storage by reducing CO_2 mobility and

* Corresponding author. Department of Physics and Technology University of Bergen, Norway.
E-mail address: tore.foyen@sintef.no (T. Føyen).

https://doi.org/10.1016/j.petrol.2020.107651
Received 12 May 2020; Received in revised form 22 June 2020; Accepted 12 July 2020
Available online 21 July 2020

stabilizing the displacement front (Enick et al., 2012; Vitoonkijvanich et al., 2015). Foam is a two-phase system consisting of gas (CO_2) dispersed in continuous thin aqueous films, called lamella, which are thermodynamically unstable and require a stabilizer (surfactants). Gas flow is impeded by lamellae which effectively decrease gas relative permeability (k_{rg}) and increase gas viscosity (μ_g). Reduction in gas permeability is caused by the trapped gas saturation (Kovscek and Radke, 1994) and increased viscosity is related to viscous shear when lamella move along pore walls (Hirasaki and Lawson, 1985) and through pore throats (Falls et al., 1989). $k_{rg}$and $\mu_g$are tied to each other through Darcy's law and cannot be measured independently during core flooding experiments, implying that it is sufficient to modify either k_{rg}or $\mu_g$to account for foam effects on CO_2 mobility. The relationship between $k_{rg}$and $\mu_g$is shown in Equation (1):

$$u_g = \frac{k k_{rg} \nabla p_g}{\mu_g} \tag{1}$$

where $u_g$is the gas flow velocity, $k$is the absolute permeability and $\nabla p_g$is the gaseous phase pressure gradient. The flow of the continuous aqueous phase is not directly affected by foam (Bernard and Jacobs, 1965; Eftekhari and Farajzadeh, 2017), therefore the water relative permeability (k_{rw}) and viscosity (μ_w) remain unchanged.

During steady-state co-injection of gas and water into a porous medium (without foam), the water saturation will adjust so that the porous medium transports the two phases at the relative rates required by the injected fluid fractions. An increase in the gas fractional flow is accommodated by a simultaneous change of both gas and water mobilities through a reduction of the water saturation and an increase in capillary pressure (Valavanides, 2018; Worthen et al., 2018).

However, an increase in gas fractional flow will not necessarily cause a reduction of water saturation during steady-state foam flow. Two distinct quality regimes of foam can exist in porous media; low-quality and high-quality regimes, separated by a transitional gas fraction f^*. When foam is in the low-quality regime, the pressure gradient adjusts to the level that the foam films can withstand, termed the limiting pressure gradient. Falls et al. (1989) assumed that there is one maximum pressure drop that any film in the porous medium can withstand. This implies that the pressure gradient should be independent of the flow rate and that the gas relative permeability increases linearly with the flow rate, exhibiting a shear thinning behaviour as elucidated by Rossen and Wang (1999).

Foam enters the high-quality regime when the gas fraction is increased above the transitional gas fraction, $f^*$and the water saturation approaches a saturation value where the lamellae are no longer stable. This occurs at a limiting capillary pressure (P_c^*) that corresponds to the maximum disjoining pressure of the foam film and is associated with a limiting water saturation for foam stability, defined as the foam breakdown saturation, S_w^*(Falls et al., 1989; Farajzadeh et al., 2015). For a foam close to its maximum disjoining pressure, a minute increase in the capillary pressure will bring a large number of films to capillary-driven rupture, so the gas fractional flow increases with virtually no saturation changes. Deviations from the above descriptions are expected in porous media because there will be a distribution of grain geometry and pore sizes influencing foam flow. The water saturation may vary over a limited range in the high-quality regime. Furthermore, variations in the maximum pressure gradient can be expected in the low-quality regime.

Alpha olefin sulfonates (AOS) are a class of anionic surfactants that are well known and widely used to generate foam with excellent foaming properties and are considered benchmark surfactants (Farajzadeh et al., 2008, 2011bib_Farajzadeh_et_al_2008bib_Farajzadeh_et_al_2011; Jones et al., 2016). This includes the large scale field test in the Snorre reservoir for hydrocarbon gas foam EOR (Blaker et al., 2002) and CO_2 foams field tests with either AOS or mixtures with AOS and other surfactants (Borling, 1994; Chou et al., 1992; Henry et al., 1996; Hoefner and Evans, 1995; Jonas et al., 1990; Moffitt et al., 2015). Anionic surfactants are only soluble in the aqueous phase, which can segregate from less dense CO_2 some distance from the well, potentially limiting the distribution of foam in the formation during field-scale operations (Vassenden et al., 1999).

Segregation of the injected surfactant can be mitigated by using surfactants soluble and transported by both the aqueous and gaseous phase. Several studies have tested various types of surfactant that partition between CO_2 and water in porous media, including: linear and branched alkylphenol ethoxylates (McLendon et al., 2012; Xing et al., 2010), branched alkyl ethoxylates (Xing et al., 2012), ethoxylated cocoamines (Chen et al., 2012), triblock copolymer surfactants (Adkins et al., 2010) and dioctyl sodium sulfosuccinates(Le et al., 2008). These studies report foam rheology measurements performed in bulk foam (Xing et al., 2010), or by flow experiments in porous media, cylindrical cores (Le et al., 2008; McLendon et al., 2012; Xing et al., 2012) and sand packs (Adkins et al., 2010; Chen et al., 2012), respectively. However, the foam experiments are challenging to generalise, compare and use for parameterization in foam models due to the injection schemes used. Additionally, the core and sand pack experiments lack saturation measurements, which are important for constructing relative permeability curves and determining key foam properties such as the foam breakdown saturation, S_w^*.

This work evaluated five commercially available non-ionic, partially CO_2-soluble surfactants (Brij L23, Igepal CO720, Tergitol NP10, Tergitol TMN10, Tergitol 15-S-9) as foam stabilizers. The primary objective was to determine the steady-state foam characteristics of the different surfactants by evaluating the mobility reduction factor (MRF) and the limiting water saturation where foam abruptly collapses (S_w^*). Partitioning between CO_2 and brine, cloud point temperature has previously been reported by Barrabino et al. (2020) and foam generation and decay during unsteady-state injection by Føyen et al. (2020). Foam measurements were obtained by co-injecting CO_2 and surfactant solutions through a sandstone core at various CO_2 flow velocities and CO_2 fractions. Gamma ray attenuation was used to accurately monitor *in-situ* saturations during steady-state co-injections. The surfactants were evaluated by considering the water saturation where foam will abruptly collapse (S_w^*) and the mobility reduction factor (MRF), describes the reduction in gas mobility by foam (see Equation (8) for details). The five partially CO_2-soluble, non-ionic surfactants were compared with the well-known and widely used water-soluble anionic AOS surfactant. The experimental observations were fitted to an implicit-texture local--equilibrium foam model developed by Vassenden and Holt (2000). The model curves aid the analyses by simplifying quantification, revealing additional observations and demonstrating the use of the dataset as input to implicit-texture local-equilibrium foam models.

2. Methods and materials

2.1. Rock material

Steady-state co-injections with CO_2 and brine or surfactant solution were performed in a single cylindrical, outcrop Bentheimer sandstone core (Table 1) to eliminate the impact of changing core properties. Porosity was determined by NaNO3 flooding. The liquid absolute permeability was calculated using Darcy's law using four constant volumetric injection rates. The core was cleaned and re-saturated with

Table 1
Core properties.

Length (cm)	19.9 ± 0.01
Diameter (cm)	3.71 ± 0.01
Pore Volume (ml)	47.8 ± 0.5
Porosity	0.22 ± 0.01
Permeability (Darcy)	2.83 ± 0 .15

surfactant solution before each separate foam injection experiment. The permeability of the core was monitored throughout the experimental campaign and negligible variations between measurements were observed.

2.2. Fluid preparation

Synthetic seawater doped with caesium (Cs-dSSW, see Table 2) was used as the aqueous phase for all co-injections and was mixed with the appropriate surfactant (Table 3) to produce surfactant solutions. Addition of Caesium improves signal-to-noise ratio during *in-situ* saturation monitoring due to increased gamma attenuation that increases the signal contrast between the aqueous phase and CO_2 at experimental conditions. All aqueous phases were filtered through a 0.45 μm cellulose acetate filter before injection through the core sample. The foaming ability of five commercially available non-ionic surfactants (Sigma-Aldrich) with different CO_2/brine partitioning coefficients (kp) were compared to a C14-16 AOS (Stepan), all listed in Table 3. A constant surfactant concentration (0.5 wt %) was used for all surfactant solutions. The surfactant solutions were flushed with argon to remove dissolved oxygen and stored under an argon atmosphere. CO_2 of 99.9999% purity was used during the co-injection experiments. Measurements of cloud point temperature and partitioning coefficient for the surfactants used in this study is previously reported by Barrabino et al. (2020).

2.3. Core preparation

The Bentheimer core plug was wrapped in nickel foil (0.025 mm) to reduce exposure between CO_2 and the Viton rubber sleeve in the carbon fibre bi-axial core holder (Fig. 1). Methanol was injected to increase pore pressure and to fill the pore space with liquid. The pore pressure was always 200 bar and the confinement pressure was 270 bar during the co-injections. The temperature was 40 °C when non-ionic surfactant solutions (CO_2-soluble surfactants) were used and 80 °C when AOS was used.

A rigorous core cleaning process was performed after each experiment to ensure that surfactant residue was removed. The cleaning started with injection of 2-propanol/water azeotrope followed by methanol, toluene and n-hexane (approximate 10 PV for each). The cleaning process summarised below also ensured 100% fluid saturation of the CO_2 saturated core ($I_{Sw=0}$) and the aqueous phase saturated core ($I_{Sw=1}$) necessary to perform the reference scans needed for *in-situ* saturation monitoring.

1 Injection of 2-propanol/water azeotrope (87.7 wt % 2-propanol)
2 Injection of methanol
3 Injection of toluene
4 Injection of n-hexane
5 Injection of CO_2
6. Record CO_2 ($I_{Sw} = 0$) reference scans
7. Injection of synthetic seawater
8 Injection of surfactant solution
9. Record brine ($I_{Sw} = 1$) reference scans (core ready for next co-injection experiment)

Table 2
Composition of caesium doped synthetic seawater. All salts were EMSURE salts (Merck Millipore) supplied by VWR.

Component	Concentration [wt. %]
Deionized water	94.52
CsCl	2.63
NaCl	1.37
$CaCl_2 \cdot 2H_2O$	0.19
$MgCl_2 \cdot 6H_2O$	0.90
KCl	0.07
Na_2SO_4	0.33

Table 3
Surfactants used as the foaming agents. Partitioning coefficients were measured at 40 °C and 200 bar (Barrabino et al., 2020).

Commercial Name	Type	kp [wt. %/wt. %]
Anionic, water-soluble		
BIO-TERGE® AS-40 (AOS)	$C_{14\text{-}16}$ sodium olefin sulfonate	0
Non-ionic, partially CO_2-soluble		
Tergitol 15-S-9	Branched alkyl ethoxylate	1.45 ± 0.14
Tergitol TMN 10	Branched alkyl ethoxylate	0.87 ± 0.01
Tergitol NP 10	Branched alkylphenol ethoxylate	0.10 ± 0.00
Igepal CO 720	Linear nonylphenol ethoxylate	0.22 ± 0.00
Brij L23	Lauryl ethoxylate.	0.02 ± 0.00

Absorption measurements were also performed when the core was saturated with surfactant solution by measurement of surfactant concentrations in the produced effluents. The surfactant analyses during Step 8 (by HPLC) showed no traces of the surfactant used in the previous experiment, indicating sufficient cleaning of the core.

2.4. Experimental procedure

Steady-state co-injections of CO_2 and surfactant solution for six different surfactants evaluated the foaming properties of each surfactant. In addition, CO_2/water relative permeability curves in the presence and absence of foam were obtained. The experimental observations provided input parameters for the foam model. Before every co-injection several pore volumes (>6) of surfactant solution were first injected to satisfy surfactant adsorption. Effluent concentrations were measured to ensure that the core was fully saturated with surfactant solution prior to starting the co-injection. The volume of surfactant solution required to satisfy adsorption varied for the different surfactants but was less than 2.0 PV (for Tergitol 15-S-9 that had the highest adsorption, 1.1 mg surfactant per gram of rock).

Foam was injected from the top of the core using four different CO_2 Darcy velocities ($u_g = 0.5$, 0.8, 1.05 and 1.3 m/day) at four different gas fractions (0.6, 0.8, 0.9 and 0.95), as indicated in the injection scheme (Fig. 2). The CO_2 velocities and gas fractions could vary slightly for the different experiments. For the experiments with Tergitol 15-S-9 only three gas fractions were used for the flow velocity 1.05 m/s. The flow rates were changed when steady-state pressures were reached. The fluid saturations were measured at steady-state using *in-situ* saturation monitoring (Chapter 2.5). The differential pressure across the core was logged versus time, using two Fuji differential pressure transmitters (range 5 and 20 bar) to calculate the foam apparent viscosity (μ_{app}), water relative permeability (k_{rw},) and CO_2 relative permeabilities with and without the presence of foam ($k^f_{rg}$and k_{rg}) using equations 3 and 4, respectively. Experimental input parameters such as core temperature, flow velocities and back- and confinement-pressures were logged versus time during co-injections. Experimental output parameters such as inlet-, outlet- and differential pressures were continuously monitored and are presented and discussed below. Data is available from an open-source online data repository hosted by Mendeley Data (Føyen and Holt, 2020).

In addition to the foam co-injections, a steady-state co-injection with CO_2 and brine was performed at five different gas fractions (0.22, 0.42, 0.60, 0.80 and 0.90) with a Darcy velocity of 2.9 m/day to obtain reference water/CO_2 relative permeability data without the presence of foam. The experimental results were fitted to the LET relative permeability curves as shown in Fig. 5.

2.5. In-situ Saturation monitoring

Aqueous (surfactant solutions and brine) and (CO_2) phase saturations were measured using gamma ray attenuation saturation monitoring. The gamma ray source and detector was located on one side of the core and the detector was directly opposite (Fig. 1). The source and

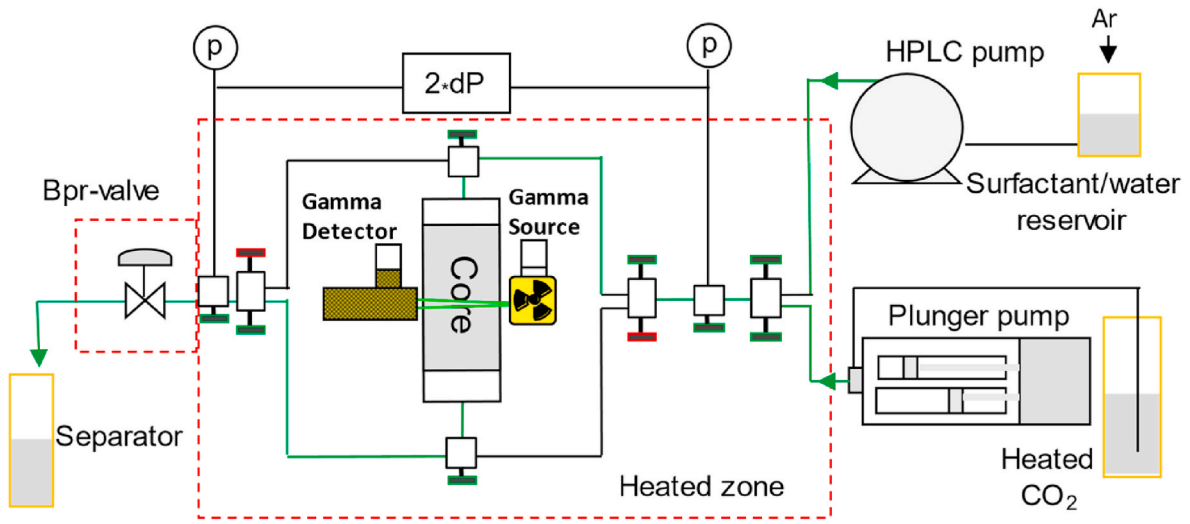

Fig. 1. Experimental setup for co-injections with CO2 and surfactant solution. CO2 from the plunger pump (Quizix Q5210) was co-injected with surfactant solution from the HPLC pump (Beckman Model 100A) through the high-pressure steel tubes (1/8 in inner diameter, marked green) and Autoclave needle valves (green for open, red for closed) to the top of the vertically positioned core sample. Produced fluids at the bottom were depressurized through the back-pressure regulator valve and collected in the separator. A gamma source and detector mounted on a motorized unit (not shown) enabled ISSM. The HPLC pump was used between co-injections to inject various solutions (brine, surfactant solutions and cleaning fluids).

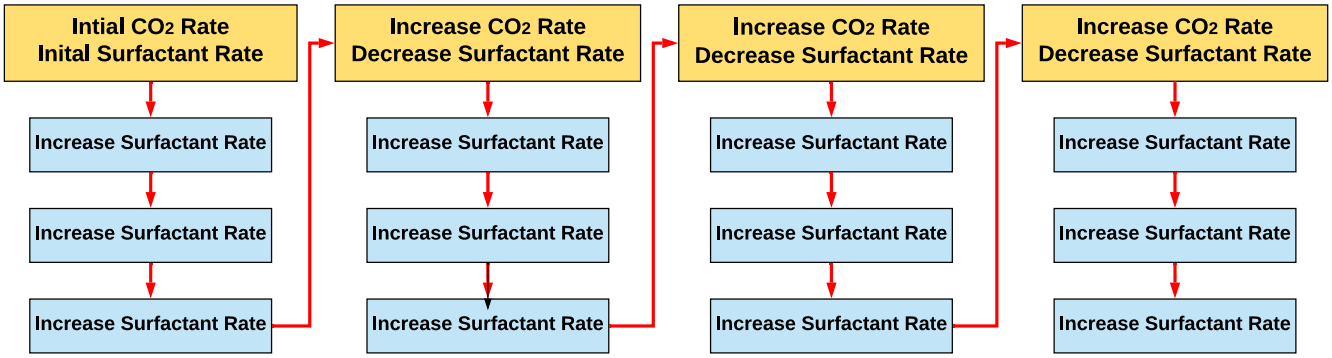

Fig. 2. The injection schemes used during the steady-state co-injections with CO_2 and surfactant solution. The unit for CO_2 Darcy velocities (u_g) is m/day.

detector pair were attached to the same motorized unit so that they could move up and down along the core for measurements at multiple predetermined positions distributed at a 5 mm distance across the core length. At each scan-location, acquisition was performed by emitting the γ-ray at a constant intensity through the core towards the detector. The intensity (counts) was recorded over a predetermined acquisition time (120 s) before the source/detector was moved to the next position. The recorded intensity (I_{Sw}) was used to calculate the phase saturation at each position using Equation (2). The calculation required two reference scans; one for each phase, obtained when the core was 100% saturated with the aqueous phase ($I_{Sw=1}$) and the gaseous phase CO_2 ($I_{Sw=0}$). The reported $S_w$is the average value for the whole core, excluding the first and last 1 cm of the core affected by interference from the end pieces of the core holder.

$$S_w = \frac{\ln\left(\frac{I_{Sw}}{I_{Sw=0}}\right)}{\ln\left(\frac{I_{Sw=1}}{I_{Sw=0}}\right)} \tag{2}$$

Reference scans (minimum one for each phase) were performed prior to co-injection to account for any differences in rock material, core location and aqueous solution composition for gamma attenuation, as recommended by Reed and Cense (2018). The saturation profiles had small capillary end effects and the complete profiles can be found in the online dataset (Føyen and Holt, 2020).

2.6. Flow equations

2.6.1. Relative permeability of water and CO_2 without foam

Co-injection of CO_2 and brine was used to calculate the CO_2/water relative permeability without foam. The relative permeability for water (k_{rw}) and gas (k_{rg}) was calculated with the Darcy equation:

$$k_{rg} = \frac{u_g{}^*\mu_g}{\mathrm{k} * \nabla p_g} \tag{3}$$

$$k_{rw} = \frac{u_w{}^*\mu_w}{\mathrm{k} * \nabla p_w}$$

andwhere $\mu_w$and μ_g, $u_w$and u_g, $\nabla p_w$and $\nabla p_g$are the viscosities, Darcy velocities and pressure gradients of the water and gas phases, respectively. Zero capillary pressure is assumed, *i.e.* $\nabla p_w = \nabla p_g$.

Experimentally obtained water and gas relative permeability (k_{rw} and k_{rg}) data were fitted to permeability curves as a function of water saturation using the empirical LET model (Lomeland et al., 2005):

$$k_{rg} = k_{rg}^{v} * \frac{(1 - S_{wn})^{L_g}}{(1 - S_{wn})^{L_g} + E_g * (S_{wn})^{T_g}} \tag{4}$$

$$k_{rw} = k^0_{rw} * \frac{(S_{wn})^{L_w}}{(S_{wn})^{L_w} + E_w * (1 - S_{wn})^{T_w}} \quad (5)$$

where k^x_{rg} and k^0_{rw} are end points relative permeabilities and Lg, Eg, T_g, Lw, E_w, and T_w are empirical fitting parameters.

The normalized water saturation S_{wn} is defined as

$$S_{wn} = \frac{S_w - S_{wi}}{1 - S_{wi} - S_{gr}} \quad (6)$$

where S_{wi} is the irreducible water saturation and S_{gr} is the residual gas saturation.

2.6.2. Relative permeability of water and CO_2 with foam

Water (k^f_{rw}) and gas (k^f_{rg}) relative permeabilities in the presence of foam were calculated by using the same procedure as above during co-injections with CO_2 and surfactant solutions. It is well established that foam reduces gas relative permeability and can be modelled by modifying the no-foam gas relative permeability (k_{rg}) by the factor FM, inversely proportional to the mobility reduction factor (MRF). The gas relative permeability in the presence of foam (k^f_{rg}) was calculated using Equation 7.

$$k^f_{rg}(S_w) = k_{rg}(S_w) * FM \quad (7)$$

Numerous foam models that implement and extrapolate core-scale laboratory data to evaluate field-scale foam behaviour are described in the literature (Ma et al., 2015). Depending on the selected foam model, *FM* can capture the influence of several parameters such as surfactant concentration, salt concentration, permeability, flow velocity, water saturation, oil saturation and composition. The experimental observations reported here were fitted to an implicit-texture local-equilibrium foam model derived by Vassenden and Holt (2000), labelled the V–H model. The V–H model was originally derived from experimental AOS co-injection data with hydrocarbon and nitrogen gas.

For the V–H foam model, FM is defined as

$$FM = e^{(S^*_w - S_w) * s_1} + \left(\frac{u_g}{u_{g0}}\right) * FM_0 * e^{(S^*_w - S_w) * s_2},\ when\ S_w > S^*_w \quad FM = 1,\ when\ S_w < S^*_w \quad (8)$$

Where S_w is the water saturation, S^*_w is the foam breakdown saturation, FM_0 is the largest mobility reduction at the reference gas Darcy flow velocity u_{g0}, u_g is the Darcy flow velocity, s_1 and s_2 are fitting parameters controlling the mobility reduction in the high and low quality regimes, respectively.

The V–H model input parameters used to calculate the gas relative permeability with foam are illustrated in Fig. 3. Below the foam breakdown saturation (S^*_w) foam will not exist (red-area) and the gas relative permeability equals the no-foam gas relative permeability (k_{rg}), shown as the red solid line. In the high-quality foam regime (yellow-area), the V–H model gives an exponential reduction in foam gas relative permeability (k^f_{rg}) where the slope is controlled by the parameter s_1 (blacked dashed lines). A round transition region truncates the high-quality regime into the low-quality regime (green-area) where the gas mobility is a factor (FM_0) lower than the gas mobility without foam at a the reference gas velocity (u_{g0}). The parameter s_2 allows the mobility reduction to vary in the low-quality regime and the term u_g/u_{g0} accounts for the shear-thinning behaviour. The water permeability with foam is assumed to be equal to the water permeability without foam.

2.6.3. Fractional flow and apparent viscosity

Foam strength during co-injections are typically reported as apparent viscosity as a function of gas fraction (Alcorn et al., 2019) and can be obtained from the relative permeability measurements using the Buckley-Leverett equation for the fractional flow curves of water and gas, f_w and f_g. To account for the foam effect, a substitution was made using the foam gas relative permeability (k^f_{rg}). Solving for gas fractional flow gives:

$$f_g = 1 - \frac{1}{1 + \frac{k^f_{rg} * \mu_w}{\mu_g * k_{rw}}} \quad (9)$$

Thus, the apparent foam viscosity can be calculated as:

$$\mu_{app} = f_g * \frac{\mu_g}{k^f_{rg}} \quad (10)$$

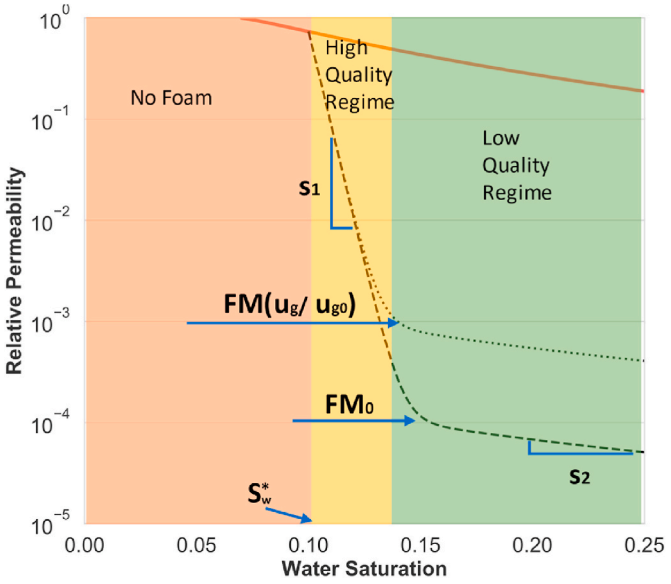

Fig. 3. Illustration of how the different V–H foam model parameters affect the gas relative permeability in the different foam regimes. Gas relative permeability without foam (red line) and with foam (black lines) using the V–H model at a reference gas velocity (dashed line) and a gas velocity $u_g > u_{g0}$ (dotted line). Values are generic but are representative for typical foam systems. Figure modified from Vassenden and Holt (2000).

2.6.4. Parameterization and coefficient of determination

A simple iterative approach was used to obtain the best fit between experimental data for the LET relative permeability model and the V–H foam model by looping through a list containing combinations of the parameters. The reported parameters were selected based on calculated errors between model curves and observed data. The conventional coefficient of determination, R^2, was used for water and CO_2 relative permeability (without foam, LET model) and was calculated by:

$$R^2 = 1 - \frac{SS_{res}}{SS_{tot}} \quad (11)$$

where, SS_{tot} is the total sum of squares, given by the mean of the observed data ($\bar{y}$) and the experimental data points (y_i):

$$SS_{tot} = \sum (y_i - \bar{y})^2 \quad (12)$$

and, SS_{res} is the sum of squares of residuals, given by the modelled values (f_i):

$$SS_{res} = \sum (y_i - f_i)^2 \quad (13)$$

For the foam model, the parameterization giving the lowest SS_{res} was used because SS_{tot} is dependent upon mean values and can become unsuitably small resulting in negative R^2 values on log scales.

3. Results and discussion

This section presents relative permeability curves for CO_2/water in the presence and absence of foam and the local-equilibrium foam model fitting to the experimental data. Data is available from an open-source online data repository hosted by Mendeley Data (Føyen and Holt, 2020).

3.1. Reference CO_2 and water relative permeability

Steady-state CO_2/water relative permeability curves provided a reference case for the CO_2 relative permeability in the presence of foam (k_{rg}^f). The V–H model foam-gas relative permeability curves were fitted to the experimental data (Fig. 4) using Equations 3 and 4 with LET parameters listed in Table 4. The low capillary number (low pressure gradient) during the co-injection without foam limited the water saturation range of the CO_2/water relative permeability data (S_w = 0.45 to 0.85) and did not overlap the saturation range (S_w = 0.10 to 0.35) observed with foam present because of the higher capillary number. The parameter $L_w$controls the shape of the water relative permeability (k_{rw}) curve at lower saturations and $L_w$was varied between 2.0 and 2.6 to achieve a model fit for CO_2 injections with foam below S_w = 0.4. The gas relative permeabilities without foam (k_{rg}) and water (k_{rw}) matched with L_w = 2.2 and were used as a reference for subsequent co-injections with foam. Other empirical parameters listed in Table 4 remained constant for all matches. For CO_2 storage decreased water saturation is beneficial, as it increases the volume occupied by CO_2.

3.2. Foam model Fitting to Experimental observations

Three physical features of foam are important to be observed in the experimental dataset and should be captured by the foam model.

i) The high- and low-quality regimes, separated by the transition gas fraction, where the mobility reduction (apparent viscosity) of foam is largest.
ii) The shear thinning behaviour in the low-quality regime, due to the limiting pressure gradient (Rossen and Wang, 1999).
iii) The abrupt reduction in foam strength in the high-quality regime, due to high capillary pressure (Falls et al., 1989).

All features were well captured using the V–H foam model for the steady-state co-injection with CO_2 and the anionic AOS surfactant (Fig. 5) using a water relative permeability curve with L_w = 2.2. The data points were obtained within the low- and the high-quality regime and the foam breakdown saturation (S_w^*) was captured together with the largest mobility reduction by foam (FM_0.). The four flow velocities show shear-thinning behaviour in the low-quality regime, captured by the term u_g/u_{g0} in the V–H model (Equation (9)).

The steady-state co-injection with CO_2 and the non-ionic Brij L23 surfactant generated foam (Fig. 6) which reduced CO_2 mobility by a factor of 1800 (Fig. 11). The low- and high-quality regimes were clearly observed during the experiment. The transition gas fraction revealed the largest mobility reduction of the foam with an abrupt reduction in foam strength beyond this point, in the high-quality regime. However, the shear-thinning behaviour in the low-quality regime was only evident at the lowest gas fractions (0.6 and 0.8). Additionally, the measured water saturations were within in a narrow range from 0.14 to 0.17 for the Brij L23 foam injection (Fig. 6), compared to 0.10 to 0.15 for the AOS foam injection (Fig. 5). The limited distribution in water saturations and lack of data points showing shear-thinning behaviour, indicate that most data points were obtained in the high-quality regime, or at the transition to the high-quality regime.

In contrast to steady-state co-injections without foam, increased gas flow velocities will not necessarily result in higher gas saturation for foam in the high-quality regime. This is because in the high-quality regime, bubble coalescence rather than changes in saturation facilitate the increased flow velocity (Vassenden and Holt, 2000). Fig. 6 (left plots) shows this behaviour, as the water saturation was nearly unchanged across the range of gas fractions and velocities. The sensitivity between water saturation and foam gas relative permeability in the high-quality regime caused challenges when using of Buckley Leverett equation to capture the gas fractional flow versus water saturation.

Fig. 7 and Fig. 8 show the results from the steady-state co-injections with Igepal CO720 (Fig. 7) and Tergitol NP10 (Fig. 8). Both experiments revealed the three physical features important to be observed. This

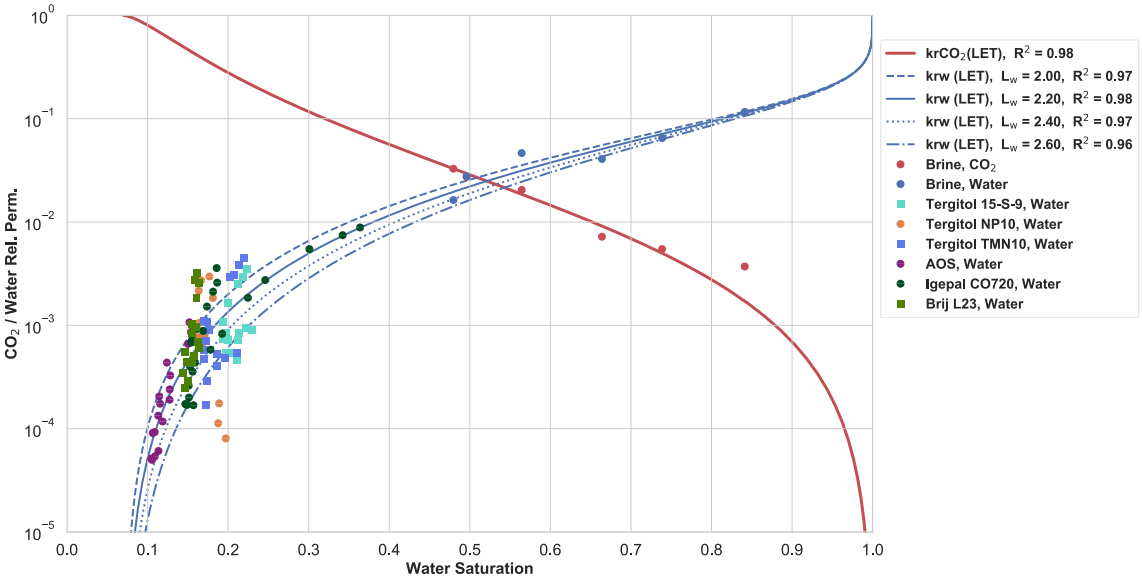

Fig. 4. Relative permeability curves (lines) for water (blue) and CO_2 (red) when fitted to the experimental data points (solid points) with and without the presence of foam. Each surfactant is identified with a unique coloured symbol. The water relative permeability parameter $L_w$was varied between 2.0 and 2.6 to produce a range of curves (in blue) fit to experimental data points, where the determination (R^2) was 0.98 for CO_2 (without foam) and ranged between 0.93 and 0.98 for water (with and without foam). Intermediate water saturation data points (S_w = 0.25 to 0.35) for surfactant Igepal CO720 were achieved with decreasing surfactant concentrations (<0.5 wt%) in a separate CO_2-injection to expand the experimental saturation range between S_w = 0.85 to 0.10 in the water relative permeability curve.

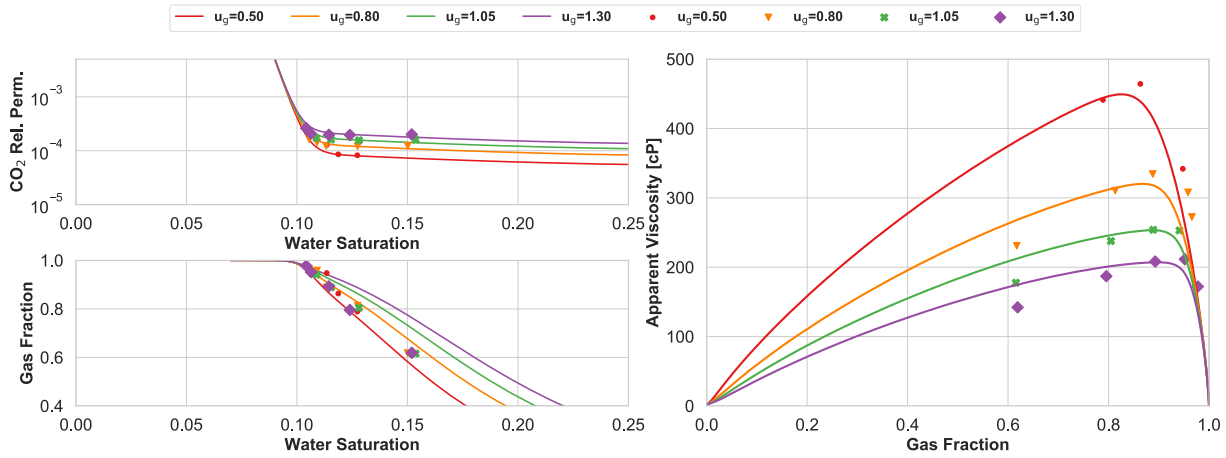

Fig. 5. Steady-state co-injection with CO_2 and the anionic AOS surfactant. The V–H model (solid lines) was matched to experimental data (symbols). Top-left: CO_2 relative permeability versus water saturation. Bottom-left: Gas fractional flow versus water saturation. Right: Apparent viscosity versus gas fractional flow. The experimental data points at different gas flow velocities are shown using unique shapes and colours. Modelled curves are shown using lines and gas flow velocities use the same colour-scheme as the experimental data points.

Table 4
LET parameters for relative permeability curves CO_2/water without foam in Fig. 4.

S_{wi}	S_{grw}	L_w	E_w	T_w	L_g	E_g	T_g
0.07	0.00	2.20	10.34	0.39	1.73	36	1.45

included the presence of a low- and high-quality foam regime, shear-thinning behaviour in the low-quality regime and an abrupt reduction in foam strength (apparent viscosity) in the high-quality regime. However, initially, the V–H model could not match the experimentally observed transition between the low- and the high-quality regimes in the apparent viscosity curves. This was due to an inadequate match between water saturation and gas fractional flow at high gas fractions. Therefore, L_w was increased to 2.4 to better reflect the water relative permeability curve for these surfactants and improved the gas fractional flow curves (see Fig. 4).

During both co-injections (Igepal CO720 and Tergitol NP10), foam gas relative permeability data points were obtained within the low- and the high-quality regime. When the necessary adjustments in the water relative permeability curve were performed, the location of the transition between the low- and high-quality regime, and the foam breakdown saturation (S_w^*) were captured. The four flow velocities, in both co-injections, showed a shear-thinning behaviour in the low-quality regime, captured by the term u_g/u_{g0} in the V–H model (Equation (9)).

Despite the improved match with small changes in water relative permeability in the presence of foam, the assumption that foam does not affect water relative permeability is considered valid. Relatively, the difference between the water relative permeability curves using L_w = 2.2 and 2.4(see Fig. 4) are small when compared with the difference between foam gas relative permeability curves (k_{rg}^f) and (no-foam) gas relative permeability curves (k_{rg}). However, the sensitivity demonstrates the importance of accurate fluid saturation measurements and reference relative permeability curves when determining foam parameters.

3.3. Non-monotonic changes in water saturation

The water saturation during steady-state co-injection is expected to decrease monotonically (or remain constant) when the gas fraction is increased, i.e. the lowest water saturation is expected at the highest gas fractions. However, this was not observed for the co-injections with

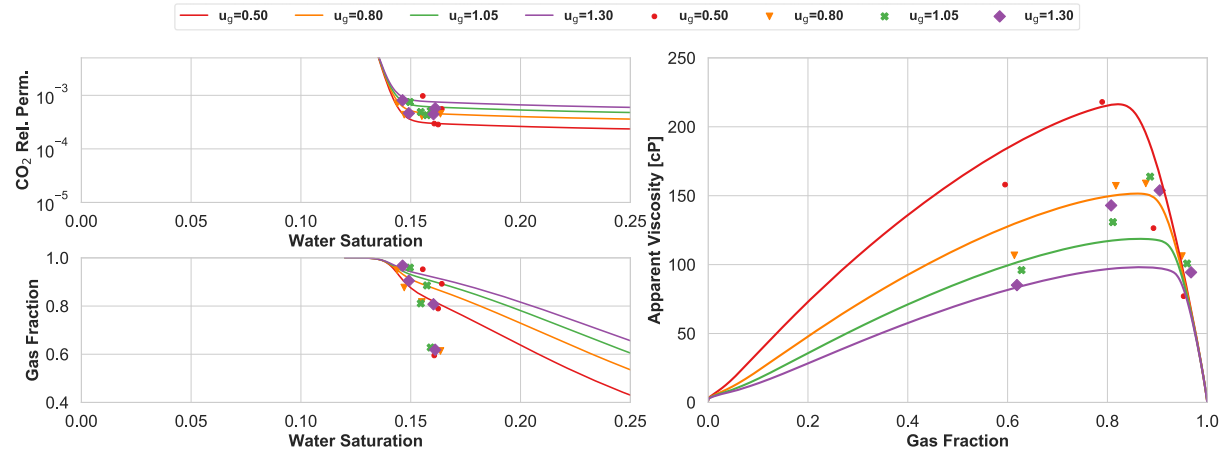

Fig. 6. Steady-state co-injection with CO_2 and the non-ionic Brij L23 surfactant. The V–H model (solid lines) was matched to experimental data (symbols). Top-left: CO_2 relative permeability versus water saturation. Bottom-left: Gas fractional flow versus water saturation. Right: Apparent viscosity versus gas fractional flow. The experimental data points at different gas flow velocities are shown using unique shapes and colours. Modelled curves are shown using lines; gas flow velocities are shown using the same colour-scheme as the experimental data points.

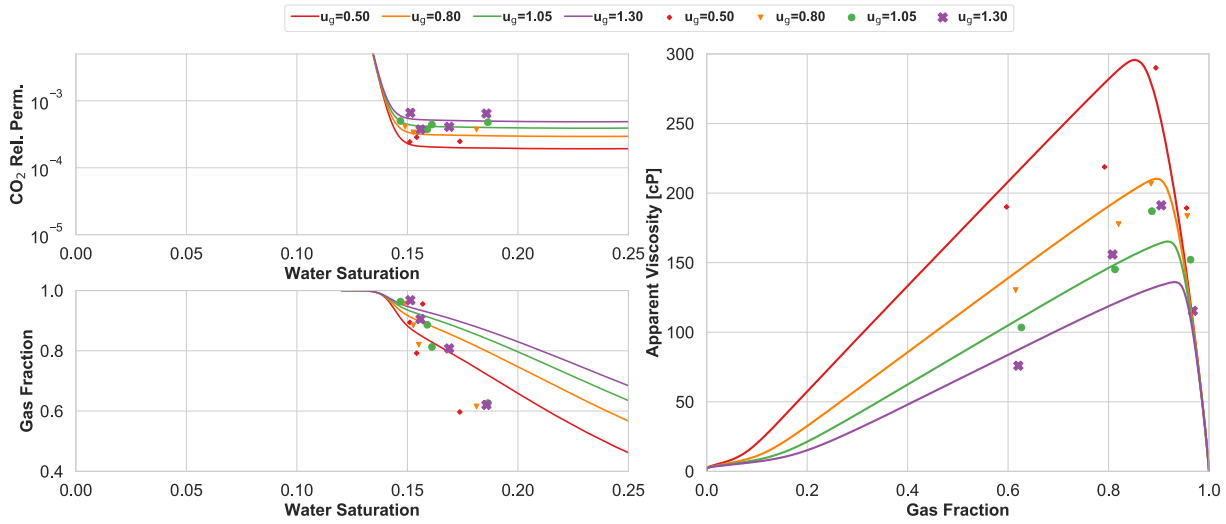

Fig. 7. Steady-state co-injection with CO_2 and the non-ionic Igepal CO720 surfactant (non-ionic). The V–H model (solid lines) was matched to experimental data (symbols) using an adjusted water relative permeability curve. Top-left: CO_2 relative permeability versus water saturation. Bottom-left: Gas fractional flow versus water saturation. Right: Apparent viscosity versus gas fractional flow. The experimental data points at different gas flow velocities are shown using unique shapes and colours. Modelled curves are shown using lines; gas flow velocities are shown using the same colour-scheme as the experimental data points.

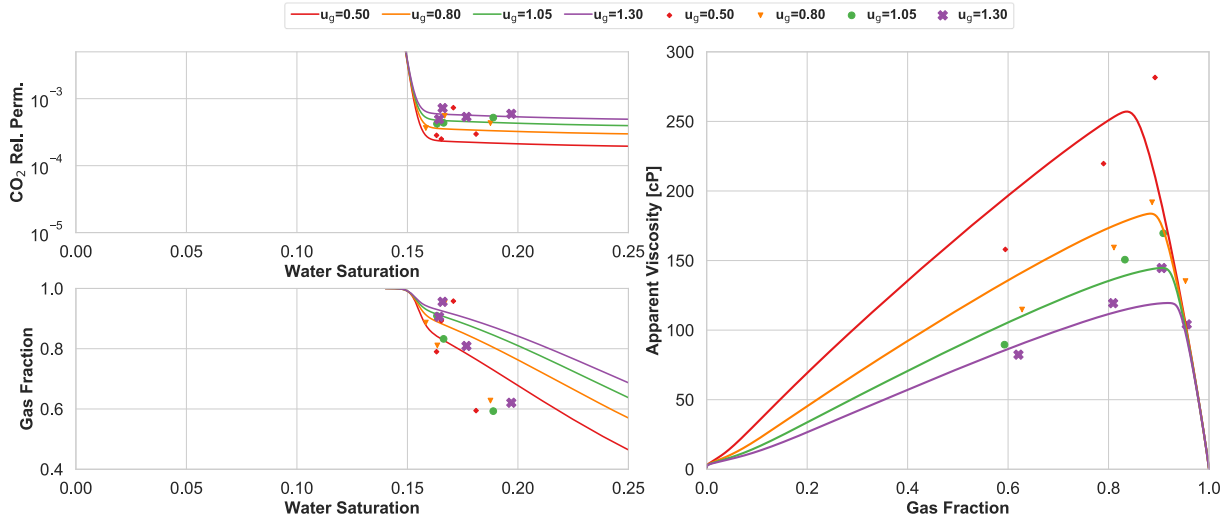

Fig. 8. Steady-state co-injection with CO_2 and the non-ionic Tergitol NP10 surfactant (non-ionic). The V–H model (solid lines) was matched with experimental data (symbols), using an adjusted water relative permeability curve. Top-left: CO_2 relative permeability versus water saturation. Bottom-left: Gas fractional flow versus water saturation. Right: Apparent viscosity versus gas fractional flow. The experimental data points at different gas flow velocities visualized using unique shapes and colours. Modelled curves are showed using lines; gas flow velocities are visualized using the same colour-scheme as the experimental data points.

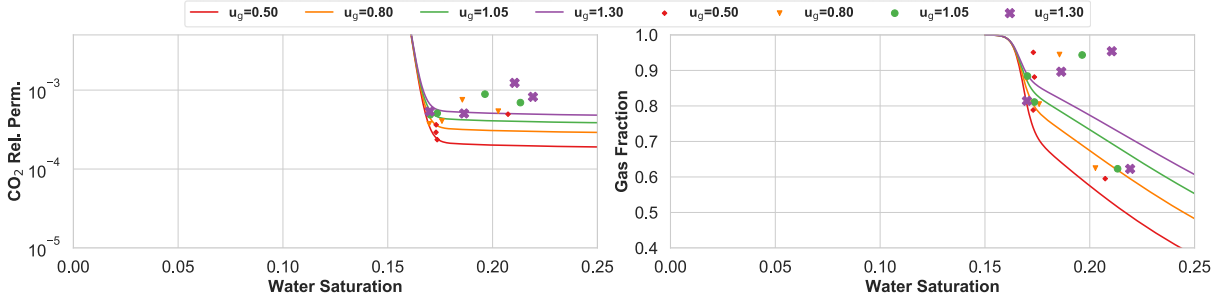

Fig. 9. Steady-state foam flood using the Tergitol TMN 10 (non-ionic). Left: Relative permeability versus water saturation. Right: Fractional flow (gas and water) versus water saturation. The experimental data points at different gas flow velocities are shown using unique shapes and colours. Modelled curves are shown using lines; gas flow velocities are shown using the same colour-scheme as the experimental data points.

Tergitol TMN 10 (Fig. 9) and Tergitol 15-S-9 (Fig. 10). Both experiments observed the lowest water saturations at the gas fraction with the lowest foam-gas relative permeability and higher water saturations were observed at both lower and higher gas fractions.

The increase in water saturation was likely caused by the reduction in CO_2 phase pressure when foam coalesced and is consistent with the difference in water saturation observed during the co-injections using surfactants (foam) and brine (reference relative permeability), due to a lower pressure gradients and associated capillary numbers (Lake et al., 2014). However, conceptually, the "limiting capillary pressure" describes an equilibrium region where increases in water saturation should cause foam regeneration and subsequent re-reduction in water, thereby maintaining a constant water saturation (Vassenden and Holt, 2000). A lack of foam regeneration when the water saturation increased may explain the observed behaviour during co-injections with Tergitol TMN 10 and Tergitol 15-S-9, indicating that the foam generation was more related to fractional flow and less to the water saturation.

The observation has implications, resulting in a relationship between the foam gas relative permeability (k_{rg}^{f}) and water saturation (S_w) that the V–H foam model (and other implicit-texture local-equilibrium foam models) cannot capture. Relative permeability curves derived from experimental data, which is used as input for reservoir scale simulations, should for each saturation have only one relative permeability, i.e. a monotonic relative permeability curve. This is evidently not the case for two foam co-injections using Tergitol TMN 10 and Tergitol 15-S-9 and the foam model fitted to the experimentally observed relative permeability data points is not applicable for reliable simulations.

3.4. Surfactant performance as foam stabilizers

All six surfactants generated foam during the steady-state co-injections, reducing CO_2 mobility by more than three orders of magnitude (Fig. 11). Four of the foam co-injections (AOS, Brij L23, Igepal CO720 and Tergitol NP10) exhibited a relationship between reduced gas relative permeability, water saturation, flow rate and gas fraction, in both the low- and high-quality regime and were capable of being captured by the V–H model (Table 5). However, two of the foam co-injections (Tergitol TMN10 and Tergitol 15-S-9), exhibited a non-monotonic change in water saturation, which the V–H foam model (and other implicit-texture local-equilibrium foam models) was not capable of capturing.

Two features obtained from the steady-state co-injections and associated model fitting are of particular interest when comparing and evaluating the performance of the surfactants as foaming agents. These include the water saturation where foam will abruptly collapse (S_w^*) and the largest MRF, which it is by definition inversely proportional to FM_0(Equation (8)). In general, a stronger foam (higher MRF) is beneficial as it improves the foam's ability to divert flow at the reservoir scale, increasing the volume of the reservoir swept during CO_2 injection.

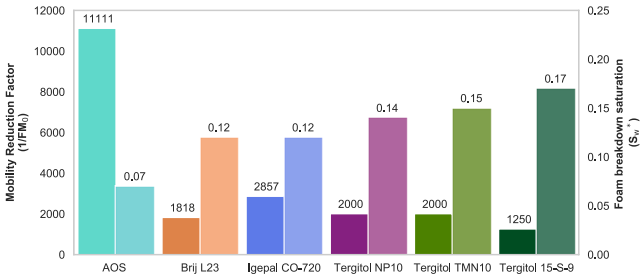

Fig. 11. Performance of the surfactants by MRF (left columns, higher is better) and foam breakdown saturation, S_w* (right columns, lower is better).

Table 5
Foam parameters and Lw values for all co-injections with surfactant solution.

Surfactant	S*	s_1	s_2	FM_0	L_w
Capable of being captured by the V–H model					
AOS	0.07	260	−7.0	0.00009	2.2
Brij L23	0.12	310	−7.0	0.00055	**2.2**
Igepal CO720	0.12	330	−9.0	0.00035	**2.4**
Tergitol NP10	0.14	500	−7.5	0.00050	**2.4**
Not capable of being captured by the V–H model					
Tergitol TMN10	0.15	400	−8.0	0.00050	**2.2**
Tergitol 15-S-9	0.17	350	−9.0	0.00080	**2.2**

However, large mobility reductions can impair injectivity. Increased foam breakdown saturation (S_w^*) improves the stability foam at high gas saturation, which is beneficial. An additional effect of foam being stable a lower water saturation is decreased residual water saturation, increasing the pore volume available for CO_2 storage.

The overview (Fig. 11) shows a clear difference in the performance between the extensively studied anionic AOS surfactant and the five non-ionic surfactants. The AOS surfactant had 4 to 10 times higher MRF and a 50% reduction in S_w^*, compared to the non-ionic surfactants. MRF accounts for the differences in temperature between the AOS surfactant co-injection (80 C°) and the non-ionic surfactant co-injections (40 C°) because the viscosity of CO_2 at the respective temperatures are included in the calculations. Despite the discrepancies in performance, secondary properties of the non-ionic surfactants such as rock absorption and being transportable by both the aqueous and gaseous phase was not considered and could outweigh the higher performance of the AOS surfactant. Complete assessments require field-scale numerical simulations using the obtained foam parameters, but also additional parameters representing concentrations, adsorption, transport, *etc*. It is interesting to observe that the two surfactants that could not be fitted to the V–H model are also the surfactants with the largest partitioning coefficients (*cf.* Table 3), *i.e.* the most CO_2 soluble surfactants. The three other non-ionic surfactants are, in this respect, more similar to the anionic AOS.

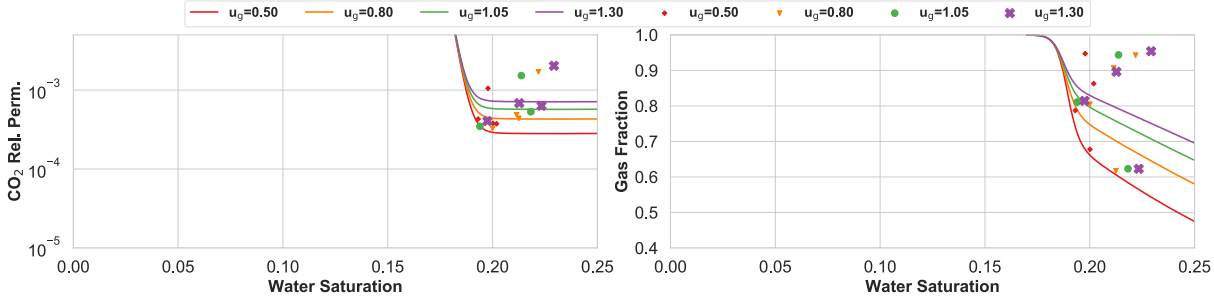

Fig. 10. Steady-state foam flood using the Tergitol 15-S-9 (non-ionic). Left: Relative permeability versus water saturation. Right: Fractional flow (gas and water) versus water saturation. The experimental data points at different gas flow velocities are shown using unique shapes and colours. Modelled curves are shown using lines; gas flow velocities are shown using the same colour-scheme as the experimental data points.

4. Conclusions

This study presented a series of steady-state co-injections of dense phase CO_2 with either anionic or non-ionic surfactant solutions at varying CO_2 flow velocities and CO_2 fractions. Six different surfactants were evaluated including the well-known anionic water-soluble AOS surfactant and five non-ionic partially CO_2-soluble surfactants. The performance of the different surfactants for stabilizing foam in porous media were evaluated by the mobility reduction factor (MRF) and the limiting water saturation where foam abruptly collapses (S_w^*).

All surfactants generated foam that reduced the mobility of CO_2 by more than three orders of magnitude. However, the AOS surfactant outperformed the non-ionic surfactants with respect to mobility reduction, exceeding a four order of magnitude reduction in MRF. The water saturations during the foam injections were significantly lower compared to the water saturations during the reference CO_2 and water relative permeability measurements due to the higher capillary number (pressure differential). An additional effect of foam being stable lower water saturations is decreased residual water saturation, which increases the pore volume available for CO_2 storage.

The V–H local-equilibrium foam model captured the experimental observations from the co-injections using the anionic AOS surfactant and three of the five non-ionic surfactants, including the reduction of foam strength in the high-quality regime and the shear-thinning flow behaviour in the low-quality regime. The model fit demonstrated the applicability of the experimental dataset for use as input into implicit-texture local-equilibrium foam models. However, two of the co-injections (Igepal CO720 and Tergitol NP10) required minute adjustments in the water relative permeability curves to achieve a model fit. Non-monotonic water saturation changes were also observed in co-injections using two of the tested surfactants (Tergitol TMN10 and Tergitol 15-S-9), which the foam model was not capable of capturing. Nonetheless, the modelling work elucidated subtle experimental trends and demonstrated the applicability of the dataset as input into implicit-texture local-equilibrium foam models.

Data availability

Datasets from the seven co-injections can be found at https://doi.org/10.17632/fz56dzr8p3.1, an open-source online data repository hosted by Mendeley Data (Føyen and Holt, 2020).

Declaration of competing interest

The authors declare that they have no known competing financial interests or personal relationships that could have appeared to influence the work reported in this paper.

CRediT authorship contribution statement

T. Føyen: Formal analysis, Visualization, Writing - original draft. **Z. P. Alcorn:** Writing - review & editing. **M.A. Fernø:** Writing - review & editing. **A. Barrabino:** Investigation, Writing - review & editing. **T. Holt:** Project administration, Investigation, Formal analysis, Writing - review & editing.

Acknowledgements

The authors wish to acknowledge the Research Council of Norway for financial support: *Improved performance of CO_2 EOR and underground storage by mobility control of CO_2* (project no. 267859 wherein all experimental work was performed); *CO2 Storage From Laboratory to On-Shore Field Pilots Using CO2-Foam for Mobility Control in CCUS* (project no. 249742); *Nanoparticles to Stabilize CO2-foam for Efficient CCUS in Challenging Reservoirs* (project no. 268216); and for funding of PhD candidate Tore Føyen

Abbreviation

AOS	Alpha olefin sulfonate
Cs-dSSW	Caesium doped synthetic seawater
CO_2	Carbon dioxide
EOR	Enhanced oil recovery
ISSM	In-situ Saturation Monitoring
V–H	Foam model, Vassenden and Holt

Symbols

f_i	Modelled value
FM	Gas mobility reduction factor
f_w and f_g	Fractional flow (water, gas)
I_{Sw}	Recorded γ-ray intensity
$I_{Sw=1}$ and $I_{Sw=0}$	Reference scans (water, gas)
kp	Partition coefficient
k	Permeability
k_{rw} and k_{rg}	Relative permeability (water, gas)
k_{rg}^f	Gas-foam relative permeability
L_g, E_g, T_g, k_{rg}^x, L_w, E_w, T_w, k_{rg}^0	Relative permeability parameters (LET)
$NaNO_3$	Sodium nitrate
P_c^*	Critical capillary pressure
∇p_w and ∇p_g	Pressure gradient (water, gas)
MRF	Mobility reduction factor
R^2	Coefficient of determination
S_1, S_2, S^*, u_{g0}, FM_0	Foam parameters (V–H model)
S_{gr}	Residual gas saturation
SS_{res}	Sum of squares of residuals
SS_{tot}	The total sum of squares

S_W	Water saturation
S_w^*	Foam breakdown saturation
S_{wn}	Normalized water saturation
S_{wi}	Irreducible water saturation
u_w and u_g	Darcy velocity (water, gas)
$\bar{y}$	Mean of the observed data
y_i	Observed data
Wt.%	Weight percentage
μ_{app}	Foam Apparent viscosity
$\mu_w$and μ_g	Viscosity (water, gas)

Appendix A. Supplementary data

Supplementary data to this article can be found online at https://doi.org/10.1016/j.petrol.2020.107651.

References

Adkins, S.S., Chen, X., Chan, I., Torino, E., Nguyen, Q.P., Sanders, A.W., Johnston, K.P., 2010. Morphology and stability of CO2-in-Water foams with nonionic hydrocarbon surfactants. Langmuir 26 (8), 5335–5348. https://doi.org/10.1021/la903663v.

Alcorn, Z.P., Fredriksen, S.B., Sharma, M., Rognmo, A.U., Føyen, T.L., Fernø, M.A., Graue, A., 2019. An integrated carbon-dioxide-foam enhanced-oil-recovery pilot program with combined carbon capture, utilization, and storage in an onshore Texas heterogeneous carbonate field. SPE Reservoir Eval. Eng. 22 (4), 1449–1466. https://doi.org/10.2118/190204-PA. SPE-190204-PA.

Barrabino, A., Holt, T., Lindeberg, E., 2020. Partitioning of non-ionic surfactants between CO2 and brine. J. Petrol. Sci. Eng. 190, 107106. https://doi.org/10.1016/j.petrol.2020.107106.

Bernard, G.G., Jacobs, W.L., 1965. Effect of foam on trapped gas saturation and on permeability of porous media to water. Soc. Petrol. Eng. J. 5 (4), 295–300. https://doi.org/10.2118/1204-PA. SPE-1204-PA,).

Blaker, T., Aarra, M.G., Skauge, A., Rasmussen, L., Celius, H.K., Martinsen, H.A., Vassenden, F., 2002. Foam for gas mobility control in the Snorre field: the FAWAG project. SPE Reservoir Eval. Eng. 5 (4), 317–323. https://doi.org/10.2118/78824-PA. SPE-78824-PA.

Borling, D., 1994. Injection conformance control case histories using gels at the wertz field CO2 tertiary flood in Wyoming. In: SPE/DOE Improved Oil Recovery Symposium. https://doi.org/10.2118/27825-MS.

Chen, Y., Elhag, A.S., Poon, B.M., Cui, L., Ma, K., Liao, S.Y., Omar, A., Worthen, A., Hirasaki, G.J., Nguyen, Q.P., Johnston, K.P., 2012. Ethoxylated cationic surfactants for CO2 EOR in high temperature. In: High Salinity Reservoirs. SPE Improved Oil Recovery Symposium, Tulsa, Oklahoma, USA. https://doi.org/10.2118/154222-MS.

Chou, S., Vasicek, S., Pisio, D., Jasek, D., Goodgame, J., 1992. CO2 foam field trial at north ward-estes. In: SPE Annual Technical Conference and Exhibition. https://doi.org/10.2118/24643-MS.

Eftekhari, A.A., Farajzadeh, R., 2017. Effect of foam on liquid phase mobility in porous media. Sci. Rep. 7 https://doi.org/10.1038/srep43870.

Enick, R.M., Olsen, D.K., Ammer, J.R., Schuller, W., 2012. Mobility and conformance control for CO2 EOR via thickeners, foams, and gels – A literature review of 40 Years of research and pilot tests. In: SPE Improved Oil Recovery Symposium, Tulsa, Oklahoma, USA. https://doi.org/10.2118/154122-MS.

Ettehadtavakkol, A., Lake, L.W., Bryant, S.L., 2014. CO2-EOR and storage design optimization. International Journal of Greenhouse Gas Control 25, 79–92. https://doi.org/10.1016/j.ijggc.2014.04.006.

Falls, A.H., Musters, J.J., Ratulowski, J., 1989. The apparent viscosity of foams in homogeneous bead packs. SPE Reservoir Eng. 4 (2), 155–164. https://doi.org/10.2118/16048-PA. SPE-16048-PA.

Farajzadeh, R., Krastev, R., Zitha, P.L.J., 2008. Foam films stabilized with alpha olefin sulfonate (AOS). Colloid. Surface. Physicochem. Eng. Aspect. 324 (1), 35–40. https://doi.org/10.1016/j.colsurfa.2008.03.024.

Farajzadeh, R., Lotfollahi, M., Eftekhari, A.A., Rossen, W.R., Hirasaki, G.J.H., 2015. Effect of permeability on implicit-texture foam model parameters and the limiting capillary pressure. Energy Fuels 29 (5), 3011–3018. https://doi.org/10.1021/acs.energyfuels.5b00248.

Farajzadeh, R., Muruganathan, R.M., Rossen, W.R., Krastev, R., 2011. Effect of gas type on foam film permeability and its implications for foam flow in porous media. Adv. Colloid Interface Sci. 168 (1), 71–78. https://doi.org/10.1016/j.cis.2011.03.005.

Føyen, T., Brattekås, B., Fernø, M.A., Barrabino, A., Holt, T., 2020. Increased CO2 storage capacity using CO2-foam. International Journal of Greenhouse Gas Control 96, 103016. https://doi.org/10.1016/j.ijggc.2020.103016.

Føyen, T., Holt, T., 2020. Dataset: CO2 mobility reduction by foam stabilized using CO2- and water-soluble surfactants. Mendeley Data. https://doi.org/10.17632/fz56dzr8p3.1.

Henry, R.L., Fisher, D.R., Pennell, S.P., Honnert, M.A., 1996. Field test of foam to reduce CO2 cycling. In: SPE/DOE Improved Oil Recovery Symposium. https://doi.org/10.2118/35402-MS.

Hirasaki, G.J., Lawson, J.B., 1985. Mechanisms of foam flow in porous media: apparent viscosity in smooth capillaries. Soc. Petrol. Eng. J. 25 (2), 176–190. https://doi.org/10.2118/12129-PA. SPE-12129-PA.

Hoefner, M., Evans, E., 1995. CO2 foam: results from four developmental field trials. SPE Reservoir Eng. 10 (4), 273–281. https://doi.org/10.2118/27787-PA.

IEA, 2018. World Energy Outlook 2018. IEA, Paris.

IPPC, 2014. Climate Change 2014: Synthesis Report. Contribution of Working Groups I, II and III to the Fifth Assessment Report of the Intergovernmental Panel on Climate Change (Geneva.

Jonas, T., Chou, S., Vasicek, S., 1990. Evaluation of a CO2 foam field trial: rangely weber sand unit. In: SPE Annual Technical Conference and Exhibition. https://doi.org/10.2118/20468-MS.

Jones, S.A., Laskaris, G., Vincent-Bonnieu, S., Farajzadeh, R., Rossen, W.R., 2016. Effect of surfactant concentration on foam: from coreflood experiments to implicit-texture foam-model parameters. J. Ind. Eng. Chem. 37, 268–276. https://doi.org/10.1016/j.jiec.2016.03.041.

Kovscek, A.R., Radke, C.J., 1994. Fundamentals of Foam Transport in Porous Media, Foams: Fundamentals and Applications in the Petroleum Industry. Advances in Chemistry. American Chemical Society, pp. 115–163.

Lake, L.W., Johns, R.T., Rossen, R.W., Pope, G.A., 2014. Fundamentals of Enhanced Oil Recovery. Society of Petroleum Engineers, Richardson, p. 496.

Le, V.Q., Nguyen, Q.P., Sanders, A., 2008. A novel foam concept with CO2 dissolved surfactants. In: SPE Symposium on Improved Oil Recovery, Tulsa, Oklahoma, USA. https://doi.org/10.2118/113370-MS.

Lee, S., Kam, S.I., 2013. Chapter 2 - enhanced oil recovery by using CO2 foams: fundamentals and field applications. In: Sheng, J.J. (Ed.), Enhanced Oil Recovery Field Case Studies. Gulf Professional Publishing, Boston, pp. 23–61.

Lindeberg, E., Grimstad, A.-A., Bergmo, P., Wessel-Berg, D., Torsæter, M., Holt, T., 2017. Large scale tertiary CO2 EOR in mature water flooded Norwegian oil fields. Energy Procedia 114, 7096–7106. https://doi.org/10.1016/j.egypro.2017.03.1851.

Lomeland, F., Ebeltoft, E., Thomas, W.H., 2005. A New Versatile Relative Permability Correlation. International Symposium of the Society of Core Analysts Toronto, Canada, Alternate A New Versatile Relative Permability Correlation.

Ma, K., Ren, G., Mateen, K., Morel, D., Cordelier, P., 2015. Modeling Techniques for Foam Flow in Porous Media. SPE-195310-PA, p. 20. https://doi.org/10.2118/169104-PA.

McLendon, W.J., Koronaios, P., McNulty, S., Enick, R.M., Biesmans, G., Miller, A.N., Salazar, L.C., Soong, Y., Romanov, V., Crandall, D., 2012. Assessment of CO2-Soluble Surfactants for Mobility Reduction Using Mobility Measurements and CT Imaging. SPE Improved Oil Recovery Symposium, Tulsa, Oklahoma, USA. https://doi.org/10.2118/154205-MS.

Moffitt, P., Pecore, D., Trees, M., Salts, G., 2015. East vacuum grayburg san andres unit, 30 Years of CO2 flooding: accomplishments, challenges and opportunities. In: SPE Annual Technical Conference and Exhibition. https://doi.org/10.2118/175000-MS.

Reed, J., Cense, A., 2018. In: Situ Saturation Monitoring (ISSM) – Recommendations for Improved Processing. International Symposium of the Society of Core Analysts, Trondheim.

Rossen, W.R., Wang, M.W., 1999. Modeling foams for acid diversion. SPE J. 4 (2), 92–100. https://doi.org/10.2118/56396-PA. SPE-56396-PA.

Valavanides, M.S., 2018. Review of steady-state two-phase flow in porous media: independent variables, universal energy efficiency map, critical flow conditions, effective characterization of flow and pore network. Transport Porous Media 123 (1), 45–99. https://doi.org/10.1007/s11242-018-1026-1.

Vassenden, F., Holt, T., 2000. Experimental foundation for relative permeability modeling of foam. SPE Reservoir Eval. Eng. 3 (2), 179–185. https://doi.org/10.2118/62506-PA. SPE-62506-PA.

Vassenden, F., Holt, T., Ghaderi, A., Solheim, A., 1999. Foam propagation on semi-reservoir scale. SPE Reservoir Eval. Eng. 2 (5), 436–441. https://doi.org/10.2118/58047-PA. SPE-58047-PA.

Vitoonkijvanich, S., AlSofi, A.M., Blunt, M.J., 2015. Design of foam-assisted carbon dioxide storage in a North Sea aquifer using streamline-based simulation. International Journal of Greenhouse Gas Control 33, 113–121. https://doi.org/10.1016/j.ijggc.2014.11.022.

Worthen, A.J., Alzobaidi, S., Tran, V., Iqbal, M., Liu, J.S., Cornell, K.A., Kim, I., DiCarlo, D.A., Bryant, S.L., Huh, C., 2018. Design of nanoparticles for generation and stabilization of CO2-in-brine foams with or without added surfactants arXiv preprint arXiv:1811.11217.

Xing, D., Wei, B., McLendon, W.J., Enick, R.M., McNulty, S., Trickett, K., Mohamed, A., Cummings, S., Eastoe, J., Rogers, S., Crandall, D., Tennant, B., McLendon, T., Romanov, V., Soong, Y., 2012. CO2-Soluble, nonionic, water-soluble surfactants that stabilize CO2-in-Brine foams. SPE J. 17 (4), 1172–1185. https://doi.org/10.2118/129907-PA. SPE-129907-PA.

Xing, D., Wei, B., Trickett, K., Mohamed, A., Eastoe, J., Soong, Y., Enick, R.M., 2010. CO2-Soluble Surfactants for Improved Mobility Control. SPE Improved Oil Recovery Symposium, Tulsa, Oklahoma, USA. https://doi.org/10.2118/129907-MS.